

Integrated gravity and topography analysis in analog models: Intraplate deformation in Iberia

Javier Fernández-Lozano,^{1,2} Dimitrios Sokoutis,^{2,3} Ernst Willingshofer,² Endre Dombrádi,^{2,4} Alfonso M. Martín,¹ Gerardo De Vicente,¹ and Sierd Cloetingh²

Received 15 March 2012; revised 9 October 2012; accepted 16 October 2012; published 12 December 2012.

[1] Trends in the topography of the Iberian Peninsula show a pronounced contrast. In the western part of the Iberian microplate the main topographic highs trend E-W to NE-SW and are periodically spaced with wavelengths of 250 km. Conversely, in the northeastern part, the region of the Iberian Chain, topography is more irregular and strike directions vary from NW-SE to E-W and NE-SW. We relate this phenomenon to shortening of a continental lithosphere, which contains two different, well-defined domains of lithospheric strength. Our hypothesis is supported by physical analog models. A new processing method has been developed to assist the interpretation of the model results. It utilizes spectral analysis of gravity and topography data derived from the experiments. Folding of the crust and mantle lithosphere yields periodic gravity fluctuations, while thickening processes lead to localized gravity lows. In this way gravity data can be used to distinguish between the two forms of lithosphere deformation and to correlate areas that underwent the same type of deformation. Gravity modeling has been performed under full in-depth control of the experimental lithosphere structure. As such, gravity signals from the models may be compared to field gravity data for better understanding the underlying deformation mechanism.

Citation: Fernández-Lozano, J., D. Sokoutis, E. Willingshofer, E. Dombrádi, A. M. Martín, G. De Vicente, and S. Cloetingh (2012), Integrated gravity and topography analysis in analog models: Intraplate deformation in Iberia, *Tectonics*, 31, TC6005, doi:10.1029/2012TC003122.

1. Introduction

[2] Several mechanisms have been suggested to explain surface uplift across relatively stable continental areas in Europe including lithosphere folding, plume activity, or tectonic inversion [e.g., Cloetingh *et al.*, 2002; Carminati *et al.*, 2009]. A frequently used method to investigate large-scale intraplate tectonics is the comparison of topography and gravity anomalies [Stephenson *et al.*, 1990; Burov and Molnar, 1998]. These studies allowed inferring mechanisms of lithosphere folding or crustal thickening through periodic and nonperiodic patterns of Bouguer anomaly and topography [Stephenson and Cloetingh, 1991].

[3] Up to now, intraplate topography in Iberia has been explained by lithosphere folding, block rotation or crustal

thickening related to thrusting [Vegas *et al.*, 1990; Fernández-Lozano *et al.*, 2011, and references therein]. However, none of these mechanisms alone can fully explain the observed topographic features on the scale of whole Iberia. Lithospheric folding as a primary form of intraplate deformation has been proposed for the Cenozoic evolution of the Iberian Peninsula. Results of numerical models [Cloetingh *et al.*, 2002] as well as recent analog models [Fernández-Lozano *et al.*, 2011] have demonstrated that coupled/decoupled modes of folding is in line with the main characteristics of the observed field gravity data and can readily explain the presence of alternating series of sedimentary basins and orogenic belts (Figure 1). Lithospheres of various thermotectonic ages comprising Iberia have been investigated independently by the numerical approach [Cloetingh *et al.*, 2002]. The applied models have presumed a laterally homogeneous crustal and mantle structure. The authors emphasized that the objective of the model series was not to reconstruct the fine details of the present-day topography but to ascertain the basic factors controlling it.

[4] These and previously published [Fernández-Lozano *et al.*, 2011] analog models on the deformation of Iberia also support the dominant role of lithospheric folding in orogen development among other proposed tectonic mechanisms. The relationship between folding and related faulting has been examined under various dynamic, geometrical and rheological conditions and the models provided a realistic subsidence and uplift pattern in

¹Departamento de Geodinámica, Facultad de Ciencias Geológicas, Universidad Complutense de Madrid-IGEO, CSIC-UCM, Madrid, Spain.

²Department of Earth Sciences, Faculty of Geosciences, Utrecht University, Utrecht, Netherlands.

³Department of Geosciences, University of Oslo, Oslo, Norway.

⁴Falcon-TXM Oil & Gas Ltd., Budapest, Hungary.

Corresponding author: D. Sokoutis, Department of Earth Sciences, Faculty of Geosciences, Utrecht University, PO Box 80 021, NL-3508 TA, Utrecht, Netherlands. (dimitrios.sokoutis@uu.nl)

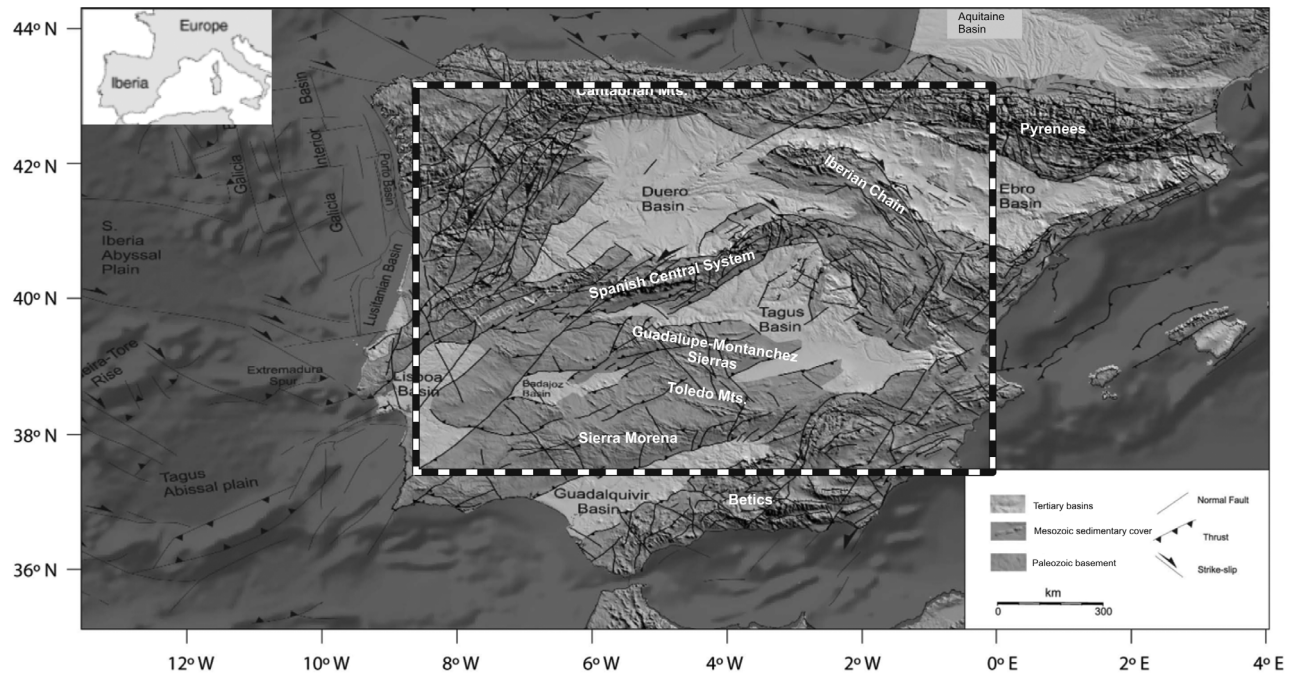


Figure 1. Digital elevation model showing the topography of the Iberian Peninsula. Large basins and mountain ranges are labeled. Main tectonic elements are also presented (modified after *Fernández-Lozano et al.* [2011]). Gray scale shading draped on the DEM indicates simplified geological units.

a laterally homogeneous setup. However, they anticipated the necessity of crustal heterogeneities for partitioning the deformation between thrusting and significant strike-slip movements.

[5] Therefore, both the rheological difference between the Variscan and Mesozoic lithosphere and preexisting zones of weakness have been implemented in the presented analog models. We examine the processes that control topography buildup in Iberia with a new experimental approach, which utilizes thickness variations and Bouguer gravity signals calculated along cross sections of analog models. Analog models provide a continuous record of topography development and by doing so reveal the prevalent type of deformation. The novelty of our experimental approach is that we correlate topography as well as gravity anomalies derived from the models with topography and field gravity data of the natural prototype. Thus we use the findings of fully controlled laboratory experiments to foster our understanding of lithosphere deformation of natural examples. We test this new method with reference to the Iberian plate demonstrating that the style of deformation and changing topographic expressions are the consequence of lateral strength variations within the lithosphere.

[6] Our results confirm the applicability of the method and demonstrate that this integrated approach can successfully be applied to any other natural laboratory regardless of its tectonic setting.

2. Geological Setting

[7] The main characteristics of the Iberian Peninsula, in terms of topography, crustal structure and rheology, taken into account in the modeling strategy are as follows. Western Iberia exhibits E-W to NE-SW oriented topographic highs, which

are crosscut by Permian structures. Among them the most prominent one is the Plasencia Fault (Figure 2a). The NE-SW fault has been described as a Late Variscan sinistral strike-slip structure intruded by a mafic dike [*Vegas, 1975, 2000; Arthaud and Matte, 1977*]. The Mesozoic evolution of the fault system has been related to the opening of the Mid-Atlantic. N-S extension of the Iberian margin [*Pinheiro et al., 1996*] led to widespread extension and intrusion of the mafic dike. Its reactivation during the Alpine orogeny is suggested by a number of studies [*Cabral, 1989; Villamor, 2002; Araújo, 2004; Vegas et al., 2004*].

[8] The eastern part of Iberia, however, shows NW-SE to NE-SW and E-W trends of topography, which seem to correlate with the orientation of the main Mesozoic rift system [*De Vicente et al., 2009*]. During the first stages of the Iberian rifting, the Somolinos Fault (Figure 2a) might have represented part of the master fault system that controlled Mesozoic sedimentation during extension [*Arche and López-Gómez, 1996*]. These types of listric structures have been described in pure shear models where hot lithospheric mantle becomes involved in deformation. Fault segments of the Somolinos Fault formed a part of the Mesozoic Iberian Rift and marked the boundary between a cold and stable Variscan lithosphere to the west and a hot Mesozoic lithosphere that includes the present-day Iberian Range. The models presented here aim to reconstruct both types of morphologic patterns that are partly related to inherited tectonic elements.

[9] Geophysical data portray Moho depths of ~ 35 km along the Spanish Central System, 45 km below the Pyrenean-Cantabrian Mountains, 35–40 km beneath the Iberian Range and ~ 38 km in the Betics. These depressions of the Moho are characterized by gravity lows indicating the presence of crustal roots underneath the main topographic highs, whereas less

pronounced gravity anomalies correlate with the main Iberian basins (Figure 1), where Moho depths are in the order of 29–30 km [Banda et al., 1981; Díaz and Gallart, 2009].

[10] Lithospheric strength models and calculations predict strong mantle rheology along the Duero and Tagus basins but low strength along the Spanish Central System [Tejero and Ruiz, 2002]. Weak rheology in the Iberian Range has been interpreted as a result of Mesozoic thermal weakening of the lithosphere due to widespread extension prior to the

Alpine orogeny [Van Wees and Stephenson, 1995]. This set of geologic and geophysical information is an essential input to design analog model series.

3. Methodology

[11] The model lithosphere representing the Iberian microplate consists of a brittle upper crust (dry feldspar sand), a ductile lower crust and a ductile lithospheric mantle (silicone mixtures). These layers float on a low-viscosity, high-density fluid simulating the asthenosphere. The experimental asthenosphere consists of a mixture of sodium polytungstate solution and glycerol with density, $\rho = 1800 \text{ kg m}^{-3}$ and viscosity $\eta = 1.2 \text{ Pa s}$. More details on the experimental procedure and the scaling analysis are given in Appendix A. The first experiments have been performed without any lateral strength variations providing a reference model (Model I). In the second series inherited weak zones (Model II) were introduced to model two preexisting structures, namely, the NW-SE trending Somolinos fault in eastern Iberia and the NE-SW oriented Plasencia Fault in the western part of the peninsula (Figure 2a). While the former marks the boundary to the weak domain in the northeastern corner of Iberia, the latter is a discrete and narrow (width of 5 mm in the model) structure. Material properties used in the experiments are listed in Table 1 and model setups are shown in Figure 2. Scaling of the experiments was done following Sokoutis et al., [2000] and Sokoutis and Willingshofer [2011]. Four-dimensional changes of the model surface were documented at regular intervals of 15 min by laser scanning. Deformation and internal structure of the model lithosphere were inferred by slicing of the model at the final stage. For 2.5-D gravity modeling, topography, thicknesses and densities of the deformed layers were taken along eight cross sections. On the basis of the established scaling ratios these output parameters were accordingly upscaled to nature.

[12] A 2.5-D gravity modeling was performed on representative cross sections using the standard Ewing-Talwani approximation for the extracted geo bodies [Talwani et al., 1959]. Spectra of Bouguer anomalies and surface variations were calculated by Fourier transform with GMT

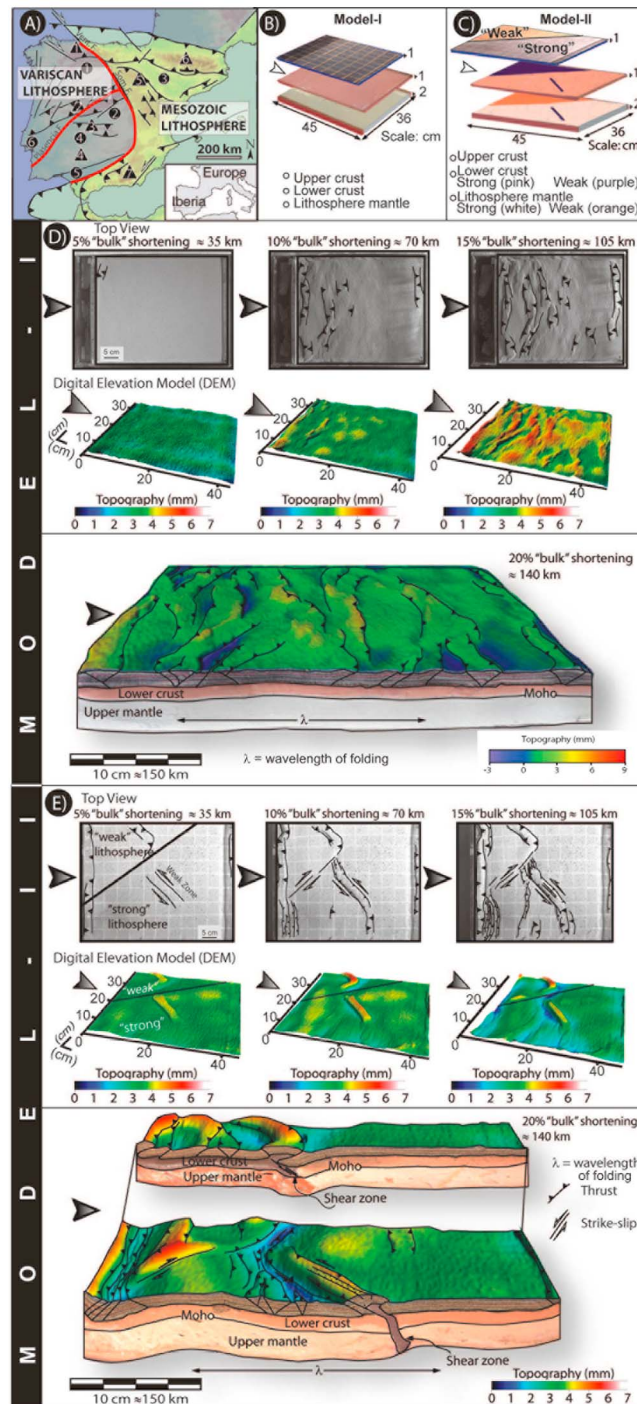


Figure 2. (a) Simplified map of Iberia showing the main lithospheric domains (strong Variscan lithosphere in purple and weak Mesozoic lithosphere in green). Circles delineate main basins: (1) Duero Basin, (2) Tagus Basin, (3) Ebro Basin, (4) Badajoz Basin, (5) Guadalquivir Basin. Triangles denote main mountain ranges: (1) Cantabrian Mountains, (2) Spanish Central System, (3) Toledo Mountains, (4) Sierra Morena, (5) Iberian Chain, (6) Pyrenees, (7) Betics. Both the contact of the Variscan and Mesozoic lithospheres in the Iberian Peninsula, including the Somolinos Fault, and the Plasencia Fault are highlighted by red solid lines. (b) Setup of Model I (homogeneous lithosphere) and (c) setup of Model II (heterogeneous lithosphere). (d and e) Experimental deformation of Models I and II, respectively, with structural interpretations of (top) top views and (middle) digital elevation models at different stages during shortening of the model and (bottom) a perspective view combining interpreted cross sections and DEMs. Arrowheads represent the direction of convergence.

Table 1. Physical Properties of the Experimental Materials Used in the Models

Layer	Density ρ (kg/m ³)	Viscosity η (Pa s)	Thickness h (m)	Length (m)	Coefficient of Friction μ	Velocity v^a (m s ⁻¹)	Cohesion (Pa)	R_m	S_m	R_{mn}/R_{mnn} S_{mn}/S_{mnn}
<i>Model I</i>										
Upper crust nature	2670	-	1.50E+04	6.6E+05	0.4	1.585E-10	6E+07	-	5.17	1.701
Upper crust model	1330	-	1.00E-02	4.4E-02	0.6	1.389E-06	35	-	3.04	
Lower crust nature	2900	1.00E+21	1.50E+04	6.6E+05	-	1.585E-10	-	1777	-	0.780
Lower crust model	1486	4.08E+04	1.00E-02	4.4E-02	-	1.389E-06	-	2278	-	
Upper lithosphere mantle nature	3400	1.00E+22	3.00E+04	6.6E+05	-	1.585E-10	-	417	-	0.778
Upper lithosphere mantle model	1606	1.87E+05	2.00E-02	4.4E-02	-	1.389E-06	-	535	-	
<i>Model II: Strong Lithosphere</i>										
Upper crust nature	2670	-	1.50E+04	6.6E+05	0.4	1.585E-10	6E+07	-	5.17	1.701
Upper crust model	1330	-	1.00E-02	4.4E-02	0.6	1.389E-06	35	-	3.04	
Lower crust nature	2900	1.00E+21	1.50E+04	6.6E+05	-	1.585E-10	-	1777	-	0.780
Lower crust model	1486	4.08E+04	1.00E-02	4.4E-02	-	1.389E-06	-	2278	-	
Upper lithosphere mantle nature	3400	1.00E+22	3.00E+04	6.6E+05	-	1.585E-10	-	417	-	0.778
Upper lithosphere mantle model	1606	1.87E+05	2.00E-02	4.4E-02	-	1.389E-06	-	535	-	
<i>Model II: Weak Lithosphere</i>										
Upper crust nature	2670	-	1.50E+04	6.6E+05	0.4	1.585E-10	6E+07	-	5.17	1.701
Upper crust model	1330	-	1.00E-02	4.4E-02	0.6	1.389E-06	35	-	3.04	
Lower crust nature	2900	1.00E+20	1.50E+04	6.6E+05	-	1.585E-10	-	17770	-	1.808
Lower crust model	1532	9.75E+03	1.00E-02	4.4E-02	-	1.389E-06	-	9829	-	
Upper lithosphere mantle nature	3400	1.00E+21	3.00E+04	6.6E+05	-	1.585E-10	-	4167	-	0.963
Upper lithosphere mantle model	1590	2.3E+04	2.00E-02	4.4E-02	-	1.389E-06	-	4325	-	

^aThe velocity v denotes the rate of convergence.

software [Wessel and Smith, 1998]. For a detailed description of the workflow, see Appendix B.

4. Modeling Results

4.1. Model I: Homogeneous Lithosphere

[13] Deformation of Model I initiated close to the moving wall and gradually propagated to more distal regions through the entire model run (Figure 2d, top). Alternating topographic highs and lows were controlled by closely spaced pop-ups and thrusts (Figure 2d). Cross sections cut from the model revealed folding and displayed a regular wavelength of the ductile layers (see example in Figure 2a (bottom)). Thrusts developing in the brittle crust were triggered at the inflection points of the fold limbs, in agreement with previous modeling results on folding of strong lithospheres [Burg et al., 1994; Sokoutis et al., 2005]. Thickness variations to the extent of 40% of the initial layer thickness occurred within the lower crust as well. The amount was dependent on the position within the developed fold. Thicker lower crust accompanied synforms, while thinner crust was observed in the antiforms.

[14] Representative profiles of topography, Moho depth and Bouguer anomaly generally share the same trend, indicating overall lithosphere folding (profiles X-X' and Y-Y', Figure 3a). However, in certain parts of the model, deviating from the folding trend, deep Moho corresponds to elevated topography thus a local minimum is found in the gravity profile. These anomalies coincide with the observed thrusts. Hence, the relative negative Bouguer anomalies can be attributed to locally thickened, brittle crust in the pop-up structures. For illustration of the differences in gravity responses to folding and to thickening over the same topography and forming a basis for discrimination between the dominant mechanisms, see Figure 4. The deviation from the ideal case, i.e., thrusts being parallel to the indenter face is due to technical limitations, which challenge producing a perfectly homogeneous sand layer. This initial perturbation does affect the spatial distribution of thrusts

to a minor extent and explains the dissimilarities between the shapes of the two profiles (Figure 3a).

[15] Spectral analyses of the model topography show short- (40–50 km) and long-wavelength (250 km) peaks (Figure 3a). However, profile Y-Y' depicts several other contributing components between 40 and 80 km and 150–250 km. Gravity profiles indicate a dominant wavelength of about 250 km that correlates with the Moho geometry. In summary, the response of the homogeneously stratified model lithosphere to shortening appears to be a combination of large-scale folding and periodic crustal thickening.

4.2. Model II: Lateral Strength Variations in the Lithosphere

[16] Consistent with the process-oriented study by Willingshofer and Sokoutis [2009], we observe that preexisting weak zones and rheological differences strongly localized deformation (Figure 2e (top), compare top view images with digital elevation models). For an amount of bulk shortening between 10% and 15%, strike-slip faults developed in the low-strength zones and later became accompanied by thrusts. Under these more complex initial conditions the stronger part of the lithosphere exhibited similar folding pattern as in the homogeneous model (Model I). However, interfering E-W and NE-SW striking structures perturbed periodic thrusting. Bouguer gravity anomalies together with topography and Moho depth variations along the entire section of the stronger part further support that the main mechanism was folding (Figure 3b, profile X-X'). However, local crustal thickness variations were also observed. For instance, high topography close to the indenter is a result of crustal thickening as indicated by the low-gravity anomaly. This phenomenon is more pronounced over the weak zone where a thick upper crustal pile evolved in the form of a pop-up structure. It correlates with a relatively deep Moho and a local minimum of Bouguer anomaly (about -300 mGal). These results indicate that the mechanically stronger lithosphere was deformed dominantly

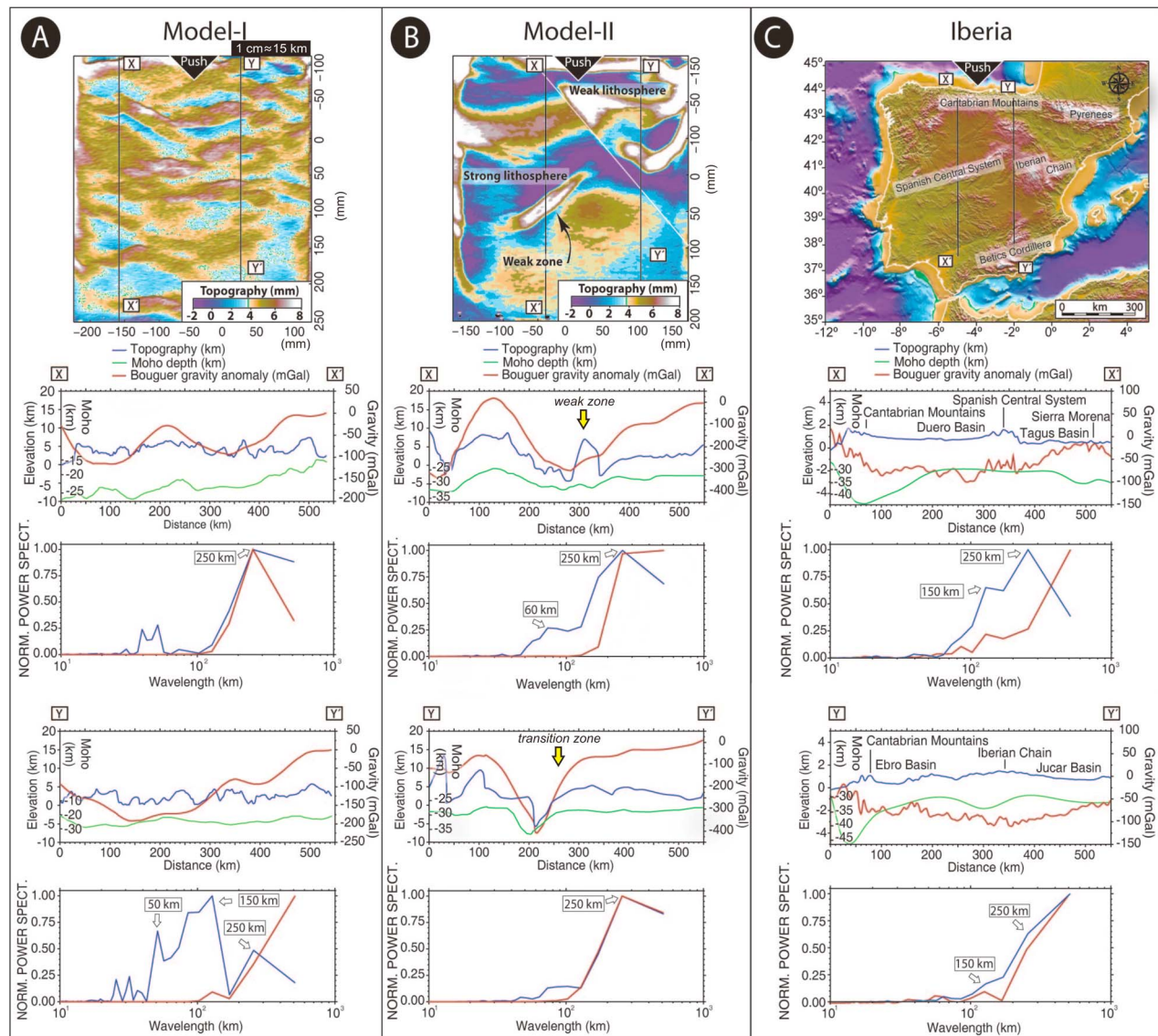


Figure 3. Comparison of selected representative profiles of topography, Moho depth, Bouguer anomaly and normalized power spectra in (a) Model I, (b) Model II and (c) Iberia microplate. Note that values from the models were scaled to nature. Black arrows represent the direction of convergence. Yellow arrows mark the weak zone and the transition zone between the two, rheologically different lithospheres.

by folding as in Model I, i.e., no significant change in the wavelength, yet slightly altered by the introduced weak zone.

[17] Differences in style of deformation occurred and manifested in pronounced topographic variations along profile Y-Y' in Figure 3b. Significantly higher peak elevation (by $\sim 15\%$) was encountered in the area characterized by low lithospheric strength than in the stronger regions (compare profiles in Figure 3b). A deep trough marks the transition from weak to strong lithosphere. Obviously such a sharp boundary cannot be expected in nature where the transition is more gradual between the Variscan and Mesozoic lithospheres. The associated deep model Moho produced a negative peak in Bouguer anomaly (-420 mGal). In the part of the model characterized by strong lithosphere (second half of profile Y-Y' in Figure 3b), deformation was hardly

observable. There, undulations of Bouguer anomaly are suppressed compared to profile X-X' in Figure 3b because strain was localized in the weaker region as portrayed by extensive thrusting and thickening and less deformation took place in the stronger part of the experimental lithosphere (Figure 2e).

[18] For the calculated normalized spectra of topography and gravity, a good correlation can be established between profiles of strong model lithospheres. They show distinct shorter (~ 60 – 80 km) and longer (150 – 250 km) dominant wavelengths of topography. The Bouguer anomaly spectrum of profile Y-Y' is very similar to that of profile X-X' with a maximum at 250 km. As a response of the folding of the mechanically stronger domain of the model, a local maximum at shorter wavelengths was anticipated in the gravity

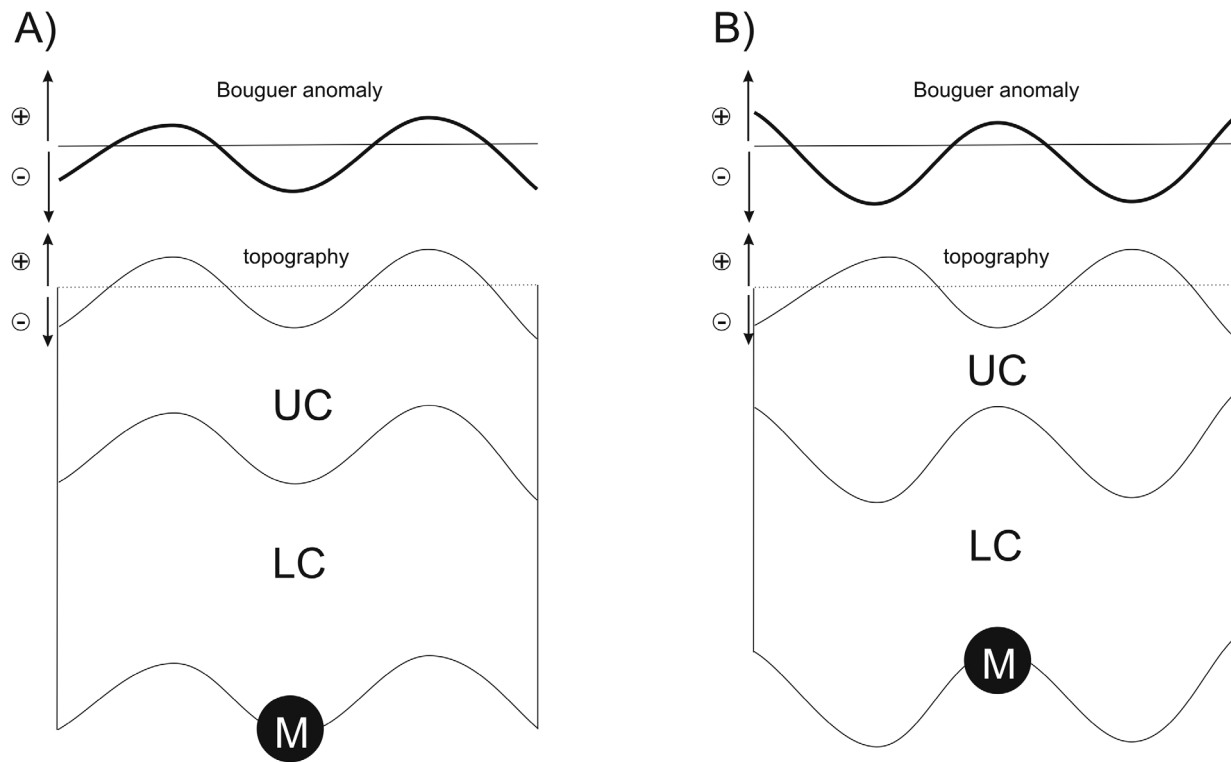


Figure 4. Cartoon illustrating difference in gravity response over the same topography in case of (a) folded crust and (b) an isostatically compensated mountain belt, i.e., thickened crust. Abbreviations used in the figure are as follows: UC = upper crust, LC = lower crust, M = Moho. Although not scaled, the relationship of deformation mechanism, structure of the crust and gravity anomaly is illustrated.

spectrum for profile Y-Y'. The similarity between the gravity spectra for X-X' and Y-Y' is most likely due to the sharp boundary between the two rheologically different domains. It creates a broad Moho depression at the central part, which is overwhelming in the Bouguer anomaly pattern and yields a half wavelength similar to that of the folded domain along X-X'. The most significant results stemming from the topography spectra is the attenuation of shorter wavelengths due to localized deformation in the weak lithosphere by thickening, which is also reflected in corresponding Moho depth and Bouguer anomaly profiles (Figure 3b, Y-Y' profile).

5. Discussion

5.1. Lithosphere Strength Variations and Topography

[19] As a result of the Iberia-Eurasia collision, large-scale folding has been advocated to shape the early Cenozoic topography of Iberia [De Vicente and Vegas, 2009]. This process is supported by periodic variations of the Moho, topography and gravity anomalies [Stephenson and Cloetingh, 1991; Burov et al., 1993; Cloetingh et al., 2002]. We have modeled folding of the lithosphere under specific rheological conditions. The simple boundary conditions introduced in the analog models obviously cannot reconstruct the full complexity of the natural prototype. However, the first-order inferences are applicable. Results have shown that the spatial distribution of the mountain ranges can be related to lateral strength variations and inherited structures. Spectral analysis has been

deployed to distinguish periodic from nonperiodic signals over large areas. As such, we used the presence/absence of periodicities as a proxy to infer the dominant mode of deformation, i.e., folding versus thickening. Evidently both topography and gravity anomalies are overestimated in the models. Erosion and lateral density variations due to igneous intrusions within the crust, not incorporated in the experiments, can account for the attenuated topography and gravity signals in the real data set compared to the model values.

[20] Based on the lithosphere deformation and related topography development observed in the physical experiments, the following mechanism is put forward to explain the evolution of western Iberia, the rheologically stronger part. At the northern and southern periphery of the peninsula, the orogens (Cantabrian Mts. and Sierra Morena, respectively) were built up by a combination of lithosphere buckling and flexural load caused by the crustal wedge. We consider the Duero Basin as a natural analog that overlays upward deflected Moho related to buckling of the lithospheric mantle. The orogen adjacent to the weak zone in Model II (profile X-X' Figures 3b and 3c) may correspond to the Spanish Central System taking into account the available existing data from this region [Tejero and Ruiz, 2002].

[21] Spectra of topography and gravity anomalies of model and nature are fairly similar. Long wavelengths (150–300 km) depict large-scale lithosphere folding, while short ones (40–80 km) are associated with thrusts. In summary, comparison of model profiles (i.e., topography, crustal thickness and gravity)

to nature suggests that the observed periodicity of the signals results from large-scale folding and superimposed thrusting within the strong lithosphere.

[22] Deformation appears to be confined to the weak lithosphere in the eastern part of the Iberian Peninsula in the form of an extensive thickening of the crust. This localization in the weak lithosphere hampers strain propagation toward the south. Lack of short-wavelength periodicity in topography and gravity spectra was inferred from the models as well as derived from the available data for Iberia. These findings suggest that instead of folding in eastern Iberia thickening has taken place and shaped the mountain belts.

5.2. The Role of Permian Structures During Cenozoic Deformation of Iberia

[23] Reactivation of preexistent zones of weakness in our models led to strike-slip displacements during N-S shortening (compare Model I to II in Figure 2). NE-SW striking faults accommodated left-lateral movements, whereas NW-SE striking faults were right-lateral. With the advance of deformation these faults became reactivated as thrusts leading to localized uplift. Natural examples with similar behavior are found along the Plasencia and Somolinos faults respectively. These observations indicate that in the presence of inherited weak zones strain partitioning affects indistinctly both the strong and weak lithospheres during Cenozoic convergence.

[24] The present-day topography in Iberia is therefore most likely the result of a combination of various previously proposed deformation mechanisms. Periodic large-scale folds across the westernmost part interfere with a series of inherited Permian faults (e.g., Plasencia fault) giving rise to E-W and NE-SW trending, regularly spaced chains of mountains. On the other hand, topography in the eastern part follows various trends. The directions are controlled by crustal thickening related to reactivation of Mesozoic rift-related structures, which localized deformation during Cenozoic (e.g., Somolinos fault).

6. Conclusions

[25] The newly developed methodology to perform spectral analyses of gravity and topography in analog models for a comparison with field data provides valuable information on the mechanism of intraplate mountain building. This approach can generally be used for tectonic modeling purposes. In the case study of Iberia, integration of gravity and topography analyses allowed us to distinguish periodic from nonperiodic patterns and to resolve the role of inherited structures on strain localization and topography buildup.

[26] The models suggest that lateral strength variations control the mode of deformation during convergence. These differences arise from lateral thermomechanical variations across Iberia and appear to profoundly determine the mode of lithosphere deformation. Folding and thickening are associated with distinctive topography and gravity signatures. As similar patterns are observable in nature, it appears that the rheology of the lithosphere has played an important role during mountain building.

[27] Consequently, the observed, mostly E-W, trending periodic topography in western Iberia is representative of folding of the entire lithosphere (250 km wavelength) and fold related thrusts (50–80 km wavelength). Thickening of

the upper and lower crust by thrusting and ductile flow, respectively, explains the formation of topographic highs in eastern Iberia.

Appendix A

A1. Experimental Procedure

[28] The experiments were performed in a rectangular Plexiglas box with transparent vertical sidewalls. One wall was mobile and acted as an indenter. The moving wall was connected to a low-frequency electric engine through a screw jack. Velocities adopted for this study are 0.5 cmh^{-1} . The three-layer models (Figure 2) consist of ductile, slightly non-Newtonian silicone mixture layers representing the upper mantle and lower crust, respectively. A K-feldspar sand layer represents the brittle upper crust. These layers, which are characterized by the properties listed in Table 1, rest on an asthenospheric material made of a mixture of polytungstate and glycerol to ensure isostatic equilibrium. The experiments have been performed under normal gravity conditions. A laser scan has been used to obtain the digital elevation model (DEM) of 0.5 mm horizontal and 0.1 mm vertical resolution combined with top view pictures taken with a digital camera at constant time rate during evolution of the model.

A2. Scaling Analysis

[29] The models were scaled following the principles of geometric and dynamic-rheologic similarity [Hubbert, 1937; Ramberg, 1981; Weijermars and Schemeling, 1986]. Rheologic–dynamic similarity was retained by scaling the gravitational stress $\sigma^* = \rho^*g^*l^*$, where ρ , g and l are the density, the gravitational acceleration and the length, respectively. The asterisk denotes the ratio between model and nature [Sokoutis *et al.*, 2000; Sokoutis and Willingshofer, 2011]. Proper scaling was tested by calculations of nondimensional numbers given by ratios between forces acting on the models [Ramberg, 1981]. For the viscous deformation, the ratio between gravitational and viscous stresses (Ramberg number R_m [Weijermars and Schemeling, 1986]) is given by

$$R_m = (\rho_d g h_d) / (\eta \dot{\epsilon}) = (\rho_d g h_d l_d) / (\eta v)$$

Density, length and thickness of the ductile layer are denoted by ρ_d , l_d and h_d , respectively, g ($=9.81 \text{ m s}^{-2}$) is the gravitational acceleration, η is the viscosity and $\dot{\epsilon}$ is the strain rate given by the ratio between the mean velocity of convergence v and the length of the ductile layer l_d . The velocity of shortening was calibrated according to our present knowledge on the rate of convergence in Iberia. For scaling brittle deformation, we considered the ratio between gravitational stress and cohesive strength (S_m , Smoluchowski number [Ramberg, 1981]):

$$S_m = (\rho_b g h_b) / (\tau_c + \mu_c \rho_b h_b)$$

where ρ_b and h_b are the density and thickness of the brittle layer, respectively, g ($=9.81 \text{ ms}^{-2}$) is the gravitational acceleration, τ_c is the cohesive strength and μ_c is the

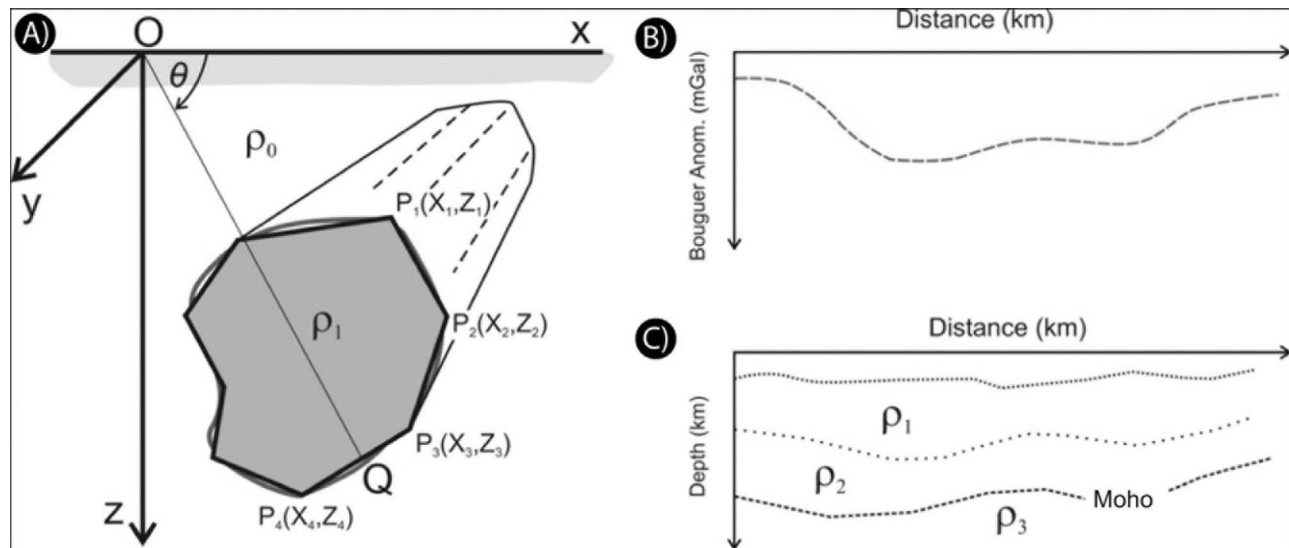


Figure B1. (a) Illustration of the Talwani method to calculate gravity anomalies applied to an irregular-shape body (modified after *Lowrie* [2007]). (b) Bouguer anomaly caused by density variations from the model cross section shown in Figure B1c. (c) Cross section obtained from analog experiment showing three different density bodies related to upper crust (ρ_1), lower crust (ρ_2) and upper lithosphere mantle (ρ_3) from top to bottom, respectively.

coefficient of internal friction. For a precise scaling, the prototype and the model must share similar R_m and S_m values. In this work, the ratios between the above dimensionless numbers of the model and nature are very close for both the brittle and ductile part (Table 1). Ideally, both model and nature must share similar R_m and R_s numbers for dynamic similarity to be fulfilled. However, a strict one to one ratio cannot be reached due to the inherent simplifications of the modeling approach and the imprecisely constrained knowledge on the rheology in nature. The applied first-order approximations are justifiable and have been employed in all experiments.

Appendix B

[30] For gravity modeling, density and geometry of the geo bodies constituting the model lithosphere had to be extracted and used as input variables. The analog experiments were deformed up to 20% of bulk shortening in both series. After completing deformation, several 2-D cross sections were cut from the model parallel to the convergence direction. Each cross section was digitized and rescaled to nature. In this way depth of the Moho was easily acquired along the cross sections. Digital elevation models (DEMs) were regularly obtained by scanning the model surface. The final DEM combined with the data along the cross sections were used to constrain thickness and geometry of each layer. Density of the applied materials (sieved sand and silicone) was measured by a regular pycnometer (Table 1, material properties) and has also been upscaled.

[31] A 2.5-D forward gravity modeling was performed along the cross sections assuming an infinite horizontal extent of the bodies perpendicular to the strike of the section (Figure B1, along y axis). In that sense, the vertical component of the gravity anomaly caused by the body can be computed by summing the contribution of infinitesimally

small horizontal line elements. Hence, the gravity anomaly can be expressed in the following form:

$$\Delta g_z = 2G\Delta\rho \oint zd\theta, \quad (\text{B1})$$

where G is the gravitational constant, ρ is the density contrast and angle θ is measured from the positive x axis to the radius connecting the line element with the origin of the coordinate system. Modeling was carried out with GMSYS software, which is based on the methods defined by *Talwani et al.* [1959] and *Talwani and Heirtzler* [1964], and applies the algorithms described by *Won and Bevis* [1987]. In this algorithm, the boundaries of the geo bodies were approximated by polygons allowing a much faster procedure to calculate the integral numerically. Gravity anomalies were derived for each successive point on the profile with 1 km spacing (model rescaled to nature). In this way, gravity profiles have become comparable to the available field data across the Iberian Peninsula.

[32] After compilation of topography and gravity data, we have calculated their power spectra as well and compared the values along several model cross sections. The spectral analysis was carried out following Welch's method [*Welch*, 1967] by grouping an average of multiple overlapped windows. Standard error was estimated according to *Bendat and Piersol* [1986]. The calculations were done using GMT software [*Wessel and Smith*, 1998].

[33] Fourier transform was applied to gravity and topography profiles in order to convert a distance function into its amplitude and phase spectra equivalent $A(f)$ and $\varphi(f)$. The analysis of these spectra aimed to identify the presence of periodicities in both topography and calculated gravity anomalies.

[34] **Acknowledgments.** This manuscript benefited from detailed comments provided by C. Faccenna, B. Guillaume and two anonymous reviewers. The study was supported by projects Consolider 2006 Topo-Iberia CSD2006-00041 and the National Research Program CGL2006-13926-C02-01-02 Topo-Iberia Foreland. D. Sokoutis, E. Willingshofer, S. Cloetingh and E. Dombradi are grateful to the Netherlands Research Center for Integrated Solid Earth Sciences (ISES), for providing support to this study.

References

- Araújo, A. (2004), Alpine tectonics in the Juromenha region (northeast Alentejo), *Comun. Geol.*, *91*, 17–36.
- Arche, A., and J. López-Gómez (1996), Origin of the Permian-Triassic Iberian Basin, central eastern Spain, *Tectonophysics*, *266*(1–4), 443–464, doi:10.1016/S0040-1951(96)00202-8.
- Arthaud, F., and P. Matte (1977), Late Paleozoic strike-slip faulting in southern Europe and northern Africa: Result of a right-lateral shear zone between the Appalachians and the Urals, *Geol. Soc. Am. Bull.*, *88*(9), 1305–1320, doi:10.1130/0016-7606(1977)88<1305:LPSFIS>2.0.CO;2.
- Banda, E., E. Suriñach, A. Aparicio, J. Sierra, and E. Ruiz de la Parte (1981), Crust and upper mantle structure of the central Iberian Meseta (Spain), *Geophys. J. Int.*, *67*, 779–789.
- Bendat, J., and A. Piersol (1986), *Random Data: Analysis and Measurement*, John Wiley, New York.
- Burg, J.-P., P. Davy, and J. Martinod (1994), Shortening of analogue models of the continental lithosphere: New hypothesis for the formation of the Tibetan Plateau, *Tectonics*, *13*(2), 475–483, doi:10.1029/93TC02738.
- Burov, E., and P. Molnar (1998), Gravity anomalies over the Ferghana Valley (central Asia) and intracontinental deformation, *J. Geophys. Res.*, *103*, 18,137–18,152, doi:10.1029/98JB01079.
- Burov, E., L. Lobkovsky, S. Cloetingh, and A. Nikishin (1993), Continental lithosphere folding in central Asia. II: Constraints from gravity and topography, *Tectonophysics*, *226*, 73–87, doi:10.1016/0040-1951(93)90111-V.
- Cabral, J. (1989), An example of intraplate neotectonic activity, Vilarica Basin, northeast Portugal, *Tectonics*, *8*(2), 285–303, doi:10.1029/TC008i002p00285.
- Carminati, E., M. Cuffaro, and C. Dogliani (2009), Cenozoic uplift of Europe, *Tectonics*, *28*, TC4016, doi:10.1029/2009TC002472.
- Cloetingh, S., E. Burov, F. Beekman, B. Andeweg, P. Andriessen, D. Garcia-Castellanos, G. De Vicente, and R. Vegas (2002), Lithospheric folding in Iberia, *Tectonics*, *21*(5), 1041, doi:10.1029/2001TC901031.
- De Vicente, G., and R. Vegas (2009), Large-scale distributed deformation controlled topography along the western Africa-Eurasia limit: Tectonic constraints, *Tectonophysics*, *474*, 124–143, doi:10.1016/j.tecto.2008.11.026.
- De Vicente, G., et al. (2009), Oblique strain partitioning and transpression on an inverted rift: The Castilian Branch of the Iberian Chain, *Tectonophysics*, *470*, 224–242, doi:10.1016/j.tecto.2008.11.003.
- Díaz, J., and J. Gallart (2009), Crustal structure beneath the Iberian Peninsula and surrounding waters: A new compilation of deep seismic sounding results, *Phys. Earth Planet. Inter.*, *173*, 181–190, doi:10.1016/j.pepi.2008.11.008.
- Fernández-Lozano, J., D. Sokoutis, E. Willingshofer, S. Cloetingh, and G. De Vicente (2011), Cenozoic deformation of Iberia: A model for intraplate mountain building and basin development based on analogue modeling, *Tectonics*, *30*, TC1001, doi:10.1029/2010TC002719.
- Hubbert, M. K. (1937), Theory of scaled models as applied to the study of geological structures, *Bull. Geol. Soc. Am.*, *48*, 1459–1520.
- Lowrie, W. (2007), *Fundamentals of Geophysics*, Cambridge Univ. Press, Cambridge, U. K., doi:10.1017/CBO9780511807107.
- Pinheiro, L., R. Wilson, R. dos Reis, R. Whitmarsh, and A. Ribeiro (1996), The Western Iberia Margin: A geophysical and geological overview, *Proc. Ocean Drill. Program*, *149*, 3–23.
- Ramberg, H. (1981), *Gravity, Deformation, and the Earth's Crust: In Theory, Experiments, and Geological Application*, 452 pp., Academic, London.
- Sokoutis, D., and E. Willingshofer (2011), Decoupling during continental collision and intra-plate deformation, *Earth Planet. Sci. Lett.*, *305*, 435–444, doi:10.1016/j.epsl.2011.03.028.
- Sokoutis, D., M. Bonini, S. Medvedev, M. Boccaletti, C. J. Talbot, and H. Koyi (2000), Indentation of a continent with a built-in thickness change: Experiment and nature, *Tectonophysics*, *320*, 243–270, doi:10.1016/S0040-1951(00)00043-3.
- Sokoutis, D., J.-P. Burg, M. Bonini, G. Corti, and S. Cloetingh (2005), Lithospheric-scale structures from the perspective of analogue continental collision, *Tectonophysics*, *406*, 1–15, doi:10.1016/j.tecto.2005.05.025.
- Stephenson, R., and S. Cloetingh (1991), Some examples and mechanical aspects of continental lithosphere folding, *Tectonophysics*, *188*, 27–37, doi:10.1016/0040-1951(91)90312-G.
- Stephenson, R., B. Ricketts, S. Cloetingh, and F. Beekman (1990), Lithosphere folds in the Eureka orogen, Arctic Canada?, *Geology*, *18*, 603–606, doi:10.1130/0091-7613(1990)018<0603:LFITEO>2.3.CO;2.
- Talwani, M., and J. Heirtzler (1964), Computation of magnetic anomalies caused by two-dimensional structures of arbitrary shape, in *Computers in the Mineral Industries*, edited by G. A. Park, *Stanford Univ. Publ. Geol. Sci.*, *9*, 464–480.
- Talwani, M., J. L. Worzel, and M. Landisman (1959), Rapid gravity computations for two-dimensional bodies with application to the Mendocino submarine fracture zone, *J. Geophys. Res.*, *64*, 49–61, doi:10.1029/JZ064i001p00049.
- Tejero, R., and J. Ruiz (2002), Thermal and mechanical structure of the central Iberian Peninsula lithosphere, *Tectonophysics*, *350*, 49–62, doi:10.1016/S0040-1951(02)00082-3.
- Van Wees, J. D., and R. A. Stephenson (1995), Quantitative modelling of basin and rheological evolution of the Iberian Basin (central Spain): Implications for lithospheric dynamics of intraplate extension and inversion, *Tectonophysics*, *252*, 163–178, doi:10.1016/0040-1951(95)00101-8.
- Vegas, R. (1975), Wrench (transcurrent) fault System of the southwestern Iberian Peninsula, paleogeographic and morphostructural implications, *Geol. Rundsch.*, *64*(1), 266–278, doi:10.1007/BF01820667.
- Vegas, R. (2000), The intrusion of the Plasencia (Messejana) dyke as part of the Circum-Atlantic Early Jurassic magmatism: Tectonic implications in the southwestern Iberian Peninsula, *Geogaceta*, *27*, 175–178.
- Vegas, R., J. Vazquez, E. Surinach, and A. Marcos (1990), Model of distributed deformation, block rotations and crustal thickening for the formation of the Spanish Central System, *Tectonophysics*, *184*, 367–378, doi:10.1016/0040-1951(90)90449-1.
- Vegas, R., G. De Vicente, A. Muñoz Martín, and R. Palomino (2004), Los corredores de fallas de regua-Verín y Vilarica: Zonas de transferencia de la deformación intraplaca en la Península Ibérica, *Geotemas*, *6*(5), 245–249.
- Villamor, M. (2002), *Cinématica Terciaria y Cuaternaria de la Falla de Alentejo-Plasencia y su influencia en la peligrosidad sísmica del interior de la Península Ibérica*, doctoral thesis, Univ. Complutense, Madrid.
- Weijermars, R., and H. Schemeling (1986), Scaling of Newtonian and non-Newtonian fluid dynamics without inertia for quantitative modeling of rock flow due to gravity (including the concept of rheological similarity), *Phys. Earth Planet. Inter.*, *43*, 316–330.
- Welch, P. (1967), The use of fast Fourier transform for the estimation of power spectra: A method based on time averaging over short, modified periodograms, *IEEE Trans. Audio Electroacoust.*, *15*, 70–73, doi:10.1109/TAU.1967.1161901.
- Wessel, P., and W. H. F. Smith (1998), New, improved version of Generic Mapping Tools released, *Eos Trans. AGU*, *79*, 579, doi:10.1029/98EO00426.
- Willingshofer, E., and D. Sokoutis (2009), Decoupling along plate boundaries: Key variable controlling the mode of deformation and the geometry of collisional mountain belts, *Geology*, *37*, 39–42, doi:10.1130/G25321A.1.
- Won, I., and M. Bevis (1987), Computing the gravitational and magnetic anomalies due to a polygon: Algorithms and FORTRAN subroutines, *Geophysics*, *52*, 232–238, doi:10.1190/1.1442298.